1 **Single-vessel cerebral blood flow fMRI to map blood velocity by phase-contrast**
2 **imaging**

3

4 Xuming Chen[1,2], Yuanyuan Jiang[3], Sangcheon Choi[1,4], Rolf Pohmann[1],
5 Klaus Scheffler[1,5], David Kleinfeld[6,7] and Xin Yu[1,3,8,*]

6 [1]High-Field Magnetic Resonance, Max Planck Institute for Biological Cybernetics, 72076
7 Tübingen, Germany.

8 [2]Department of Neurology, Wuhan University, Renmin Hospital, Wuhan 430060, China.

9 [3]Athinoula A. Martinos Center for Biomedical Imaging, Massachusetts General Hospital and
10 Harvard Medical School, Charlestown 02129 MA, USA.

11 [4]Graduate Training Centre of Neuroscience, International Max Planck Research School,
12 University of Tübingen, 72074 Tübingen, Germany.

13 [5]Department for Biomedical Magnetic Resonance, University of Tübingen, Tübingen, Germany.

14 [6]Department of Physics, University of California at San Diego, La Jolla, CA, 92093 USA.

15 [7]Section of Neurobiology, University of California at San Diego, La Jolla, CA, 92093 USA.

16

17

18

19

20

21

22

23

24

25

26

27 [8]Lead Contact:

28 Address: Max-Planck-Ring. 11, 72076, Tübingen, Germany

29 Phone: +49 7071 601-740

30 Fax: +49 7071 601-701

31 *Correspondence: xin.yu@tuebingen.mpg.de; xyu9@mgh.harvard.edu
32

33 **Abstract**

34 Current approaches to high-field fMRI provide two means to map hemodynamics at the

35 level of single vessels in the brain. One is through changes in deoxyhemoglobin in

36 venules, i.e., blood oxygenation level-dependent (BOLD) fMRI, while the second is

37 through changes in arteriole diameter, i.e., cerebral blood volume (CBV) fMRI. Here we

38 introduce cerebral blood flow (CBF)-fMRI, which uses high-resolution phase-contrast MRI

39 to form velocity measurements of flow and demonstrate CBF-fMRI in single penetrating

40 microvessels across rat parietal cortex. In contrast to the venule-dominated BOLD and

41 arteriole-dominated CBV fMRI signal, the phase-contrast -based CBF signal changes are

42 highly comparable from both arterioles and venules. Thus, we have developed a single-

43 vessel fMRI platform to map the BOLD, CBV, and CBF from penetrating microvessels

44 throughout the cortex. This high-resolution single-vessel fMRI mapping scheme not only

45 enables the vessel-specific hemodynamic mapping in diseased animal models but also

46 presents a translational potential to map vascular dementia in diseased or injured human

47 brains with ultra-high field fMRI.

48

49

50

51

52

53

54

55 **Summary**

56 We established a high-resolution PC-based single-vessel velocity mapping method using

57 the high field MRI. This PC-based micro-vessel velocity measurement enables the

58 development of the single-vessel CBF-fMRI method. In particular, in contrast to the

59 arteriole-dominated CBV and venule-dominated BOLD responses, the CBF-fMRI shows

60 similar velocity changes in penetrating arterioles and venules in activated brain regions.

61 Thus, we have built a noninvasive single-vessel fMRI mapping scheme for BOLD, CBV,

62 and CBF hemodynamic parameter measurements in animals.

63

64

Introduction

68   Cerebral blood flow (CBF) is a key readout of neuronal processing and viability in normal

69   and diseased brain states[1]. Changes in CBF may be monitored directly within individual

70   blood vessels through the use of optical-based particle tracking techniques[2]. A variety of

71   imaging methods have been developed to measure CBF across multiple spatial scales

72   from capillary beds to the vascular network in animal brains, including multi-photon

73   microscopy[3], near-infrared spectroscopy (NIRS)[4], optical coherence tomography[5],

74   optoacoustic imaging[6], or laser doppler and speckle imaging[7, 8]. In particular, the doppler-

75   based functional ultrasound imaging method provides a unique advantage to detect the

76   CBF in the brain with a high spatiotemporal resolution, which can be readily applied for

77   awake animal imaging[9-11]. However, these methods share a common barrier that the

78   spectrum-specific signal transmission cannot effectively pass the skull of animals without

79   significant loss of the signal-to-noise ratio (SNR). Typically, a craniotomy or procedure to

80   thin the skull is needed to detect the hemodynamic signal[2]. While current techniques

81   support transcranial imaging into the superficial layers of the cortex, only functional MRI

82   (fMRI) provides a noninvasive approach for measuring hemodynamic signals throughout

83   the brain.

84   Changes in CBF may be detected by fMRI based on arterial spin labeling (ASL),

85   in which water protons in a major upstream vessel are spin-polarized with an external

86   field[12-14]. Two other fMRI-based techniques provide indirect information about changes in

87   CBF. Blood oxygenation level-dependent (BOLD) fMRI is used to determine changes in

88   the ratio of deoxy- to oxyhemoglobin in the blood and is a measure of changes in brain

89   metabolism[12, 15, 16]. Cerebral blood volume (CBV) fMRI is used to measure changes in

90   blood volume, i.e., essentially changes the diameter of arterioles, based on the use of

91   exogenous or endogenous contrast agents to differentiate blood from brain tissue[12, 17].

92   Phase-contrast (PC) MRI relies on gradient-oriented dephasing of magnetized

93   protons to map the velocity, i.e., direction and speed, of blood flow[18, 19]. The ASL-based

94   CBF fMRI technique detects local changes in the flow of blood through brain tissue but

95   does not show orientation-specific information related to the alignment of vessels[20]. Past

96   works with 7 T MR scanning showed that PC-MRI can be used to measure flow in the

97   perforating arteries through the while matter or the lenticulostriate arteries in the basal

98   ganglia of human brains[21-24]. However, the SNR was insufficient in these prior studies to

99   map changes in flow, and thus changes in CBF.

100   Here, we report on a PC-MRI method to detect the vessel-specific changes in

101   blood velocity in single trials. Compared with past implementations of PC-MRI[21, 25-28], we

102   have implemented a small surface radio frequency (RF) coil with the high field MRI, i.e.,

103   14.1 T for improved SNR. This further allows us to map the BOLD- and CBV-fMRI from

104   individual penetrating venules and arterioles, which span 20 to 70 µm diameter, with high

105   spatial resolution[29-31].

106   **Results**

107   **Phantom validation of high-resolution PC-based flow velocity measurement**

108   For calibration, we constructed an *in vitro* capillary tubing circulatory system to mimic

109   penetrating vessels, with flow rates from 1 to 10 mm/s (**Figure 1A**). A 2D PC-MRI slice is

110   aligned perpendicular to the capillary tubing (**Figure 1A, B)** and provides a voxel-specific

111   measurement of the flow velocity through two tubes with the upward flow (positive sign,

112   bright dots in **Figure 1B**) and two tubes with the downward flow (negative sign, dark dots

113   in **Figure 1B**), as well as a control tube. We observe a monotonic and near-linear relation

114 between the velocity measured by PC-MRI and the true velocity: V_{meas} =

115 (0.67 ± 0.01) $_{Vpump}$ + (0.02 ± 0.11) mm/s at echo time (TE) = 5.0 ms (**Figure 1C**). The

116 small offset could be caused by eddy current effects and other gradient-related scaling

117 errors of the PC-MRI sequence[32-34]. We further observe that the measured velocities are

118 relatively insensitive to the value of TE (**Figure 1C**).

119 We implemented the high-resolution PC-MRI for *in vivo* measurement of blood flow

120 from individual penetrating arterioles and venules through the infragranular cortex, i.e.,

121 layer V, of the anesthetized rats with 14.1 T MR scanning. To improve the SNR of PC-

122 MRI images as well as multi-gradient echo (MGE) images used for arteriole-venule (A-V)

123 mapping[29, 31], a surface RF transceiver coil with 6 mm diameter was constructed and

124 attached to the rat skull (**Supplemental Figure 1**). This was essential for the high-

125 resolution mapping with a fast sampling rate of the single-vessel flow velocity over a

126 complete hemisphere of the rat brain (**Figure 2A and Supplemental Figure 1E**).

127 ***In vivo* PC-based flow velocity mapping of penetrating microvessels**

128 We first acquired the single-vessel A-V map by aligning a 500 μm thick 2D MRI slice

129 perpendicular to the penetrating vessels through layer V of one hemisphere (**Figure 2A,**

130 **B**). We designed the pulse sequence for PC-MRI to achieve the same slice geometry of

131 the A-V map so that the CBF deduced from PC-MRI signals could be overlaid with

132 individual penetrating arterioles and venules in the single-vessel flow velocity map

133 (**Figure 2A, C**). The arteriole blood flows down into the cortex while the venule blood

134 flows upward, which determines the sign of the flow velocity. Vessel-specific velocities

135 were plotted as a function of the normalized signal intensity in the A-V map and

136 corroborated our ability to determine flow velocity specific to arterioles and venules

137 (**Figure 2C, D**). The measured flow velocities range from 1 to 10 mm/s, as previously

6

138   measured with optical methods[35]. To probe the reliability of the single-vessel MR-based

139   flow velocity method, we compared the velocities detected by PC-MRI methods with

140   different TEs and flip angles (FAs) and observed comparable results across a range of

141   parameters (**Supplemental Figure 2**). All told, these data demonstrate the feasibility of

142   *in vivo* single-vessel blood velocity mapping with the PC-based MRI method.

143   **PC-based CBF-fMRI from individual arterioles and venules**

144   We contrasted the complementary capabilities of PC-based CBF-fMRI against the signals

145   observed with the balanced steady-state free precession (bSSFP)-based single- vessel

146   BOLD- and CBV-fMRI mapping method[29] (**Figure 3**). We first created an A-V map

147   through the deep layers of the forepaw region of the primary somatosensory cortex

148   (**Figure 3Ai**), followed by 2D-bSSFP to detect stimulus-induced changes in the single-

149   vessel BOLD-fMRI signal (**Figure 3Aii**). We next performed single-vessel PC-MRI flow

150   velocity measurements with 100 x100 µm^2 in-plane resolution, a sampling rate of 4 s

151   repetition time (TR) per image, and the same geometry as the 2D-bSSFP method to

152   measure baseline flow in penetrating arterioles and venules (**Figure 3Aiii**). Changes in

153   CBF upon stimulation overlapped with individual penetrating vessels in the A-V map

154   (**Figure 3Aiv**). Lastly, we performed 2D-bSSFP for single-vessel CBV-fMRI mapping by

155   intravenous injection of iron particles into the blood in the same rats (**Figure 3Av**). The

156   BOLD-fMRI signal is primarily detected from individual penetrating venules while the

157   CBV-weighted signal is mainly located at the individual penetrating arterioles (dark dots

158   in **Figure 3Aii** with bright dots in **Figure 3Av**). In contrast, the CBF-fMRI signal is

159   observed in both penetrating arterioles and venules (**Figure 3Aiv**).

160   The stimulus-evoked responses of all three fMRI signals were studied with an

161   on/off block design (**Figures 3B-E**). Group analysis shows that the positive BOLD signal

162   from venule voxels is significantly higher than the arteriole-specific BOLD signal

163   (**Figure 3C**). In contrast, the arteriole dilation leads to an earlier CBV-weighted negative

164   fMRI signal, which is much stronger and faster than the signal from passive venule-

165   dilation (**Figure 3C**), as expected[36, 37]. Group analysis shows the similar temporal

166   dynamics of CBF changes appearing as a ramp in both arterioles and venules

167   (**Figure 3E**). The CBF-fMRI signal appears as the integral of the stimulus, i.e., a triangular

168   ramp (**Figure 3E**), compared to the saturation-like BOLD and CBV responses

169   (**Figure 3C**). The voxel-wise hemodynamic changes of BOLD, CBV, and CBF are

170   illustrated in **Supplementary Figure 3** and **movie 1**.

Discussion

172   Despite the existing tools developed for CBF measurement in both animal and human

173   brains, it remains challenging to detect the flow dynamics of intracortical micro-vessels

174   non-invasively. Here, we not only optimized the PC-MRI to map the vectorized single-

175   vessel flow velocity of penetrating arterioles and venules but also developed the single-

176   vessel CBF-fMRI based on the direct flow velocity measurement in rat brains. By

177   combining with previously established single-vessel BOLD- and CBV-fMRI methods, the

178   PC-based single-vessel CBF-fMRI method complements the scheme to map the vessel-

179   specific hemodynamic responses with high-resolution fMRI.

180   In contrast to the conventional ASL methods, PC-based MRI mapping allows

181   arterioles and venules to be distinguished for simultaneous velocity measurements

182   through a 2D plane. Also, ASL has less vascular specificity because water exchange

183   through the blood-brain barrier of capillary beds increases the weighting of the ASL-based

184   flow signal for parenchyma voxels[38, 39]. Furthermore, there is significant variability in the

185   transit time to flow from arterioles to venules through the capillary bed[40], which

186   complicates the distinction of arterioles and venules by simple ASL-based CBF mapping.

187   We detected the velocity from penetrating microvessels in the deep cortical layers with

188   PC-MRI, showing velocity values from 1 to 5 mm/s (Fig 2). Single-digit velocity (mm/s) of

189   red blood cells from cortical surface microvessels has been detected in the anesthetized

190   rats using two-photon microscopy[2, 35]. It is noteworthy that the PC-based vessel velocity

191   measurement is based on measuring water protons in blood but not limited to the flow of

192   red blood cells. Still, the PC-based velocity from microvessels matches well with the

193   previous optical measurement. We conclude that high-resolution PC-MRI is ideal for

194   noninvasive single-vessel CBF-fMRI mapping.

195   A remaining complication with PC-MRI mapping is the presence of small offsets in

196   velocity from the phantom capillary tubing with circulating flow under different conditions.

197   The phase-dependent velocity encoding depends on the quality of the magnetic field

198   gradients, and mismatched eddy currents of multiple gradients with opposite polarities,

199   as well as the nonlinear and distorted gradient fields, could contribute to distortions in

200   gradients[32-34]. In particular, the high-resolution PC-MRI method is a high-duty cycle

201   sequence and slight heating of the gradient coil during scanning may alter the gradient

202   performance, consistent with the baseline-drift of the CBF-fMRI signal in the first 5

203   minutes of scanning (**Figure 3D**). Nevertheless, it should be noted that the percentage

204   velocity changes from individual arterioles and venules can be readily detected with the

205   PC-based CBF-fMRI measurement regardless of the gradient-heating related baseline

9

206   drift. Another factor that contributes to the phase-dependent velocity error originated from

207   the limited spatial resolution of the PC-MRI images compared to the diameters of small

208   vessels[27], although corrections are possible[21, 28]. Despite the potential partial volume

209   contribution to the single-vessel BOLD, CBV, and CBF-fMRI, the vessel-specific mapping

210   scheme presents a translational potential to identify vascular dementia in diseased or

211   injured brains with ultra-high field fMRI.

ACKNOWLEDGMENTS

AUTHOR CONTRIBUTIONS

224   X.Y. and D.K. initiated the concept; X.Y. designed the research; X.C. and X.Y. performed animal

225   experiments; X.C., Y.J. performed data analysis; P.R., K.S., S.C. provided technical support; X.Y.,

226   D.K., X.C., Y.J. wrote the paper.

227

228

Methods

Design of a phantom capillary tubing flow system

In order to validate the PC-MRI sequence, a plastic circulatory flow phantom composed of the capillary tubing (PE-10, Instech Laboratories, inner diameter 210 μm) was constructed to mimic the geometries of cortical blood vessels (**Figure 1A**). The capillary tube was connected to a programmable syringe infusion/withdraw pump (Pump Elite 11, Harvard Apparatus) with an infusion rate of 0.25, 0.5, 1.0, 1.5, 2.0 ml/h, which were transferred to the flow velocity of the capillary tubing as shown in **Figure 1**. The flowing medium is a manganese solution (50 mM $MnCl_2$, Sigma-Aldrich). The phantom tube was cast with Fomblin (Sigma-Aldrich) to avoid the potential air interface artifacts.

Animal preparation for fMRI

All surgical and experimental procedures were approved by the local authorities (Regierungspraesidium, Tübingen Referat 35, Veterinärwesen, Leiter Dr. Maas) and were in full compliance with the guidelines of the European Community (EUVD 86/609/EEC) for the care and use of laboratory animals. The experimental animals were Sprague-Dawley male rats, ~ 250 g, provided by the Charles River Laboratories in Germany. Fifteen rats were used in all experiments (the evoked bSSFP-BOLD/CBV and PC-MRI signals were acquired from five of these fifteen rats).

Detailed descriptions of the surgery are given in previous publications[29, 30]. Briefly, rats were first anesthetized with isoflurane (5% induction, 1~2% maintenance), each rat was orally intubated with a mechanical ventilator (SAR-830, CWE). The femoral artery and vein were catheterized with plastic catheters (PE-50, Instech Laboratories) to monitor the arterial blood gas, administrate drugs, and constantly measure the blood pressure.

11

252   After catheterization, rats were secured in a stereotaxic apparatus, a custom-made RF

253   coil was fixed above the skull with cyanoacrylate glue (454, Loctite). After surgery,

254   isoflurane was switched off and a bolus of α-chloralose (80 mg/kg, Sigma-Aldrich) was

255   intravenously injected. A mixture of α-chloralose (26.5 mg/kg/h) and the muscle relaxant

256   (pancuronium bromide, 2 mg/kg/h) was continuously infused to maintain the anesthesia

257   and minimize the motion artifacts. Throughout the whole experiment, the rectal

258   temperature of rats was maintained at 37°C by using a feedback heating system. All

259   relevant physiological parameters were constantly monitored during imaging, including

260   heart rate, rectal temperature, arterial blood pressure, the pressure of the tidal ventilation,

261   and end-tidal CO_2. Arterial blood gases were checked to guide the physiological status

262   adjustments by changing the respiratory volume or administering sodium bicarbonate

263   (NaBic 8.4 %, Braun) to maintain normal pH levels. Dextran-coated iron oxide particles

264   (15 ~ 20 mg of Fe/kg, BioPAL, MA) were intravenously injected for CBV-weighted signal

265   acquisition.

266   **fMRI setup**

267   All images were acquired with a 14.1 T, 26 cm horizontal bore magnet (Magnex Scientific)

268   interfaced through the Bruker Advance III console (Bruker Corporation). The scanner is

269   equipped with a 12 cm magnet gradient set capable of providing a strength of 100 G/cm

270   and a 150 μs rise time (Resonance Research Inc.). A custom-made transceiver coil with

271   an internal diameter of 6 mm was used for fMRI images acquisition. For the electrical

272   stimulation, two custom-made needle electrodes were placed on the forepaw area of the

273   rats to deliver the electrical pulse sequences (330 μs duration at 1.0 ~ 2.0 mA. The pulses

274   repeated at 3 Hz for 10 s) by using a stimulus isolator (A365, WPI). The stimulation

275   duration and frequency were triggered directly through the MRI scanner which controlled

12

276   by Master-9 A.M.P.I system (Jerusalem, Israel). The triggering pulses from the MRI

277   scanner were also recorded by the Biopac system (MP150, Biopac Systems, USA).

Single-vessel multi-gradient echo (MGE) imaging

279   To anatomically map the individual arterioles and venules penetrating the deep cortical

280   layers of the somatosensory cortex, a 2D MGE sequence was applied with the following

281   parameters: TR = 50 ms; TE = 2.5, 5.0, 7.5, 10.0, 12.5 and 15.0 ms; flip angle (FA) = 55°;

282   matrix = 192 x 192; in-plane resolution = 50 x 50 μm^2; slice thickness = 500 μm. The A-V

283   map was made by averaging the MGE images from the second TE echo to the fifth TE

284   echo. In the A-V map, the arteriole voxels show bright (red marks) due to the in-flow effect

285   and venule voxels show as dark dots (blue marks) because of the fast T_2^* decay

286   (**Figure 2B**).

Balanced steady-state free precession (bSSFP) BOLD- and CBV-fMRI

288   The bSSFP sequence was applied to acquire the evoked BOLD signals by using the

289   following parameters: TR = 15.6 ms; TE = 7.8 ms; flip angle = 15°; matrix = 96 x 96; FOV

290   = 9.6 x 9.6 mm; in-plane resolution = 100 x 100 μm^2; slice thickness =500 μm. For the

291   bSSFP CBV-fMRI, the parameters were adjusted with TR = 10.4 ms and TE = 5.2 ms.

292   The total TR to acquire each image is 1 s. To reach the steady-state, 300 dummy scans

293   were used, followed by 25 pre-stimulation scans, one scan during stimulation, and 44

294   post-stimulation scans with 10 epochs for each trial. The fMRI stimuli block design of each

295   trial consisted of 10 s stimulation and 35 s inter-stimulus interval. The total acquisition

296   duration of each trial was 7 min 55 s. CBV-weighted fMRI signals were acquired after

297   intravenous injection of dextran-coated iron oxide particles (15 ~ 20 mg of Fe/kg, BioPAL,

298   MA).

Phase Contrast (PC)-MRI

To measure the flow velocity of individual arterioles and venules, the PC-MRI sequence was applied with the following parameters. For the *in vitro* phantom measurement: TR = 15.6 ms; TE = 4.2, 4.5, 5.0, 6.0 ms; flip angle = 25°; FOV = 6.4 x 6.4 mm; matrix = 128 x 128; in-plane resolution = 50 x 50 µm^2; slice thickness = 500 µm; maximum velocity (Venc) = 1.56 or 0.66 cm/s (based on the flow values); number of averages = 172. The total acquisition time was 11 min 28 s. For the *in vivo* measurements: TR = 15.6 ms; TE = 5 ms; flip angle = 30°; FOV = 6.4 x 6.4 mm; matrix = 64 x 64; in-plane resolution = 100 x 100 µm^2; slice thickness = 500 µm. A total TR for each image is 4 s. The total acquisition duration of each trial was 16 min. To measure the blood flow velocity, bipolar flow encoding gradients were applied along the slice encoding direction. The slice position was anatomically identical with the slice position of the MGE imaging.

Data analysis and statistics

All data preprocessing and analysis were performed by using the software package, Analysis of Functional NeuroImages (AFNI) (NIH, Bethesda). All relevant fMRI analysis source codes can be downloaded from https://www.afni.nimh.nih.gov/afni/.

Definition of the individual vessels

The individual arteriole/venule voxels were defined by the signal intensity of the A-V map[31]. The arterioles are determined if the voxel intensities are higher than the mean signal intensities plus two times the standard deviation of the local area in a 5 x 5 kernel. The venules are determined if the voxel intensities are lower than the mean signal intensities minus two times the standard deviation of the local area[29-31]. The locations of individual arteriole/venule voxels defined in A-V map were used to extract the time courses of BOLD/CBV-fMRI for individual vessels.

323 **BOLD/CBV-fMRI and PC-MRI data analysis**

324 To register the evoked bSSFP-fMRI images and evoked PC-MRI images with the 2D

325 anatomical A-V map, the tag-based registration method was applied. Twelve to fifteen

326 tags were selected from the averaged bSSFP-fMRI images or the averaged PC-fMRI

327 images to register those selected from A-V map. We used a 3dLocalstat AFNI function to

328 normalize the signal intensity of the single-vessel maps. This process allowed us to plot

329 the PC-based velocity values of individual vessel voxels to the normalized signal intensity

330 of A-V maps. For the evoked signals, the bSSFP-fMRI images and PC-MRI images were

331 normalized by scaling the baseline to 100. Multiple trials of block-design time courses

332 were averaged for each animal. No additional smoothing step was applied. The β-value

333 was calculated to measure the amplitude of the fMRI responses at each TR. The voxel-

334 wise β-map was illustrated with the spatial pattern of the fMRI responses corresponding

335 to the different time points after the stimulus onset. After registration (tag-based

336 registration) and region of interest extraction (3dLocalstat function, mask shown in

337 **Figure 2B**), we extracted the PC-based flow velocity values from individual vessel voxels,

338 which were identified based on the algorithm as described in the previous section.

339 The hemodynamic response function is based on the "block function" of 3dDeconvolve

340 module developed in AFNI. The HRF model is defined as follows:

341
$$h(t) = \int_0^{\min(t,L)} s^4 e^{-s}/[4^4 e^{-4}] \, ds$$

342 Gamma variate function = $s^4 e^{-s} /4^4 e^{-4}$. L was the duration of the response. BLOCK (L, 1)

343 is a convolution of a square wave of duration L, makes a peak amplitude of block

344 response = 1.

15

345   For the group analysis, Student's t-test was performed, error bars are displayed as the

346   means ± SEM. The p values < 0.05 were considered statistically significant. The sample

347   size of animal experiments is not previously estimated. No blinding and randomization

348   design was needed in this work.

349   **References**

350   1.   Attwell, D. et al. Glial and neuronal control of brain blood flow. *Nature* **468**, 232-243 (2010).
351   2.   Shih, A.Y. et al. Two-photon microscopy as a tool to study blood flow and neurovascular
352   coupling in the rodent brain. *J Cereb Blood Flow Metab* **32**, 1277-1309 (2012).
353   3.   Kleinfeld, D., Mitra, P.P., Helmchen, F. & Denk, W. Fluctuations and stimulus-induced
354   changes in blood flow observed in individual capillaries in layers 2 through 4 of rat
355   neocortex. *Proceedings of the National Academy of Sciences of the United States of*
356   *America* **95**, 15741-15746 (1998).
357   4.   Jobsis, F.F. Noninvasive, infrared monitoring of cerebral and myocardial oxygen
358   sufficiency and circulatory parameters. *Science* **198**, 1264-1267 (1977).
359   5.   Srinivasan, V.J. et al. Depth-resolved microscopy of cortical hemodynamics with optical
360   coherence tomography. *Optics letters* **34**, 3086-3088 (2009).
361   6.   Yao, J., Maslov, K.I., Shi, Y., Taber, L.A. & Wang, L.V. In vivo photoacoustic imaging of
362   transverse blood flow by using Doppler broadening of bandwidth. *Optics letters* **35**, 1419-
363   1421 (2010).
364   7.   Ances, B.M., Greenberg, J.H. & Detre, J.A. Laser doppler imaging of activation-flow
365   coupling in the rat somatosensory cortex. *NeuroImage* **10**, 716-723 (1999).
366   8.   Dunn, A.K., Bolay, H., Moskowitz, M.A. & Boas, D.A. Dynamic imaging of cerebral blood
367   flow using laser speckle. *Journal of cerebral blood flow and metabolism : official journal of*
368   *the International Society of Cerebral Blood Flow and Metabolism* **21**, 195-201 (2001).
369   9.   Mace, E. et al. Functional ultrasound imaging of the brain. *Nature methods* **8**, 662-664
370   (2011).
371   10.   Sieu, L.A. et al. EEG and functional ultrasound imaging in mobile rats. *Nature methods*
372   **12**, 831-834 (2015).
373   11.   Rungta, R.L., Osmanski, B.F., Boido, D., Tanter, M. & Charpak, S. Light controls cerebral
374   blood flow in naive animals. *Nature communications* **8**, 14191 (2017).
375   12.   Kwong, K.K. et al. Dynamic magnetic resonance imaging of human brain activity during
376   primary sensory stimulation. *Proceedings of the National Academy of Sciences of the*
377   *United States of America* **89**, 5675-5679 (1992).
378   13.   Detre, J.A., Leigh, J.S., Williams, D.S. & Koretsky, A.P. Perfusion imaging. *Magnetic*
379   *resonance in medicine : official journal of the Society of Magnetic Resonance in Medicine*
380   */ Society of Magnetic Resonance in Medicine* **23**, 37-45 (1992).
381   14.   Williams, D.S., Detre, J.A., Leigh, J.S. & Koretsky, A.P. Magnetic resonance imaging of
382   perfusion using spin inversion of arterial water. *Proceedings of the National Academy of*
383   *Sciences of the United States of America* **89**, 212-216 (1992).
384   15.   Ogawa, S., Lee, T.M., Kay, A.R. & Tank, D.W. Brain magnetic resonance imaging with
385   contrast dependent on blood oxygenation. *Proceedings of the National Academy of*
386   *Sciences of the United States of America* **87**, 9868-9872 (1990).
387   16.   Ogawa, S. et al. Intrinsic signal changes accompanying sensory stimulation: functional
388   brain mapping with magnetic resonance imaging. *Proceedings of the National Academy*
389   *of Sciences of the United States of America* **89**, 5951-5955 (1992).

390 17. Belliveau, J.W. et al. Functional mapping of the human visual cortex by magnetic
391   resonance imaging. *Science* **254**, 716-719 (1991).

392 18. Moran, P.R. A flow velocity zeugmatographic interlace for NMR imaging in humans.
393   *Magnetic resonance imaging* **1**, 197-203 (1982).

394 19. Bryant, D.J., Payne, J.A., Firmin, D.N. & Longmore, D.B. Measurement of flow with NMR
395   imaging using a gradient pulse and phase difference technique. *Journal of computer*
396   *assisted tomography* **8**, 588-593 (1984).

397 20. Detre, J.A. & Wang, J. Technical aspects and utility of fMRI using BOLD and ASL. *Clin*
398   *Neurophysiol* **113**, 621-634 (2002).

399 21. Zong, X. & Lin, W. Quantitative phase contrast MRI of penetrating arteries in centrum
400   semiovale at 7T. *NeuroImage* **195**, 463-474 (2019).

401 22. Bouvy, W.H. et al. Assessment of blood flow velocity and pulsatility in cerebral perforating
402   arteries with 7-T quantitative flow MRI. *NMR in biomedicine* **29**, 1295-1304 (2016).

403 23. Kang, C.K. et al. Velocity measurement of microvessels using phase-contrast magnetic
404   resonance angiography at 7 Tesla MRI. *Magnetic resonance in medicine : official journal*
405   *of the Society of Magnetic Resonance in Medicine / Society of Magnetic Resonance in*
406   *Medicine* **75**, 1640-1646 (2016).

407 24. Schnerr, R.S. et al. Pulsatility of Lenticulostriate Arteries Assessed by 7 Tesla Flow MRI-
408   Measurement, Reproducibility, and Applicability to Aging Effect. *Front Physiol* **8**, 961
409   (2017).

410 25. Wei, Z. et al. Optimization of phase-contrast MRI for the estimation of global cerebral blood
411   flow of mice at 11.7T. *Magnetic resonance in medicine : official journal of the Society of*
412   *Magnetic Resonance in Medicine / Society of Magnetic Resonance in Medicine* **81**, 2566-
413   2575 (2019).

414 26. Dolui, S. et al. Comparison of non-invasive MRI measurements of cerebral blood flow in
415   a large multisite cohort. *Journal of cerebral blood flow and metabolism : official journal of*
416   *the International Society of Cerebral Blood Flow and Metabolism* **36**, 1244-1256 (2016).

417 27. Geurts, L.J. et al. Vascular reactivity in small cerebral perforating arteries with 7T phase
418   contrast MRI - A proof of concept study. *NeuroImage* **172**, 470-477 (2018).

419 28. Hoogeveen, R.M., Bakker, C.J. & Viergever, M.A. MR phase-contrast flow measurement
420   with limited spatial resolution in small vessels: value of model-based image analysis.
421   *Magnetic resonance in medicine : official journal of the Society of Magnetic Resonance in*
422   *Medicine / Society of Magnetic Resonance in Medicine* **41**, 520-528 (1999).

423 29. He, Y. et al. Ultra-Slow Single-Vessel BOLD and CBV-Based fMRI Spatiotemporal
424   Dynamics and Their Correlation with Neuronal Intracellular Calcium Signals. *Neuron* **97**,
425   925-939 e925 (2018).

426 30. Chen, X. et al. Mapping optogenetically-driven single-vessel fMRI with concurrent
427   neuronal calcium recordings in the rat hippocampus. *Nature communications* **10**, 5239
428   (2019).

429 31. Yu, X. et al. Sensory and optogenetically driven single-vessel fMRI. *Nature methods* **13**,
430   337-340 (2016).

431 32. Walker, P.G. et al. Semiautomated method for noise reduction and background phase
432   error correction in MR phase velocity data. *Journal of magnetic resonance imaging : JMRI*
433   **3**, 521-530 (1993).

434 33. Peeters, J.M., Bos, C. & Bakker, C.J. Analysis and correction of gradient nonlinearity and
435   B0 inhomogeneity related scaling errors in two-dimensional phase contrast flow
436   measurements. *Magnetic resonance in medicine : official journal of the Society of*
437   *Magnetic Resonance in Medicine / Society of Magnetic Resonance in Medicine* **53**, 126-
438   133 (2005).

439   34. Bernstein, M.A. et al. Concomitant gradient terms in phase contrast MR: analysis and
440   correction. *Magnetic resonance in medicine : official journal of the Society of Magnetic*
441   *Resonance in Medicine / Society of Magnetic Resonance in Medicine* **39**, 300-308 (1998).
442   35. Schaffer, C.B. et al. Two-photon imaging of cortical surface microvessels reveals a robust
443   redistribution in blood flow after vascular occlusion. *PLoS Biol* **4**, e22 (2006).
444   36. Silva, A.C., Koretsky, A.P. & Duyn, J.H. Functional MRI impulse response for BOLD and
445   CBV contrast in rat somatosensory cortex. *Magnet Reson Med* **57**, 1110-1118 (2007).
446   37. Drew, P.J., Shih, A.Y. & Kleinfeld, D. Fluctuating and sensory-induced vasodynamics in
447   rodent cortex extend arteriole capacity. *Proc. Natl. Acad. Sci. USA* **108**, 8473-8478 (2011).
448   38. Koretsky, A.P. Early development of arterial spin labeling to measure regional brain blood
449   flow by MRI. *NeuroImage* **62**, 602-607 (2012).
450   39. Wang, J., Fernandez-Seara, M.A., Wang, S. & St Lawrence, K.S. When perfusion meets
451   diffusion: in vivo measurement of water permeability in human brain. *Journal of cerebral*
452   *blood flow and metabolism : official journal of the International Society of Cerebral Blood*
453   *Flow and Metabolism* **27**, 839-849 (2007).
454   40. Hutchinson, E.B., Stefanovic, B., Koretsky, A.P. & Silva, A.C. Spatial flow-volume
455   dissociation of the cerebral microcirculatory response to mild hypercapnia. *NeuroImage*
456   **32**, 520-530 (2006).
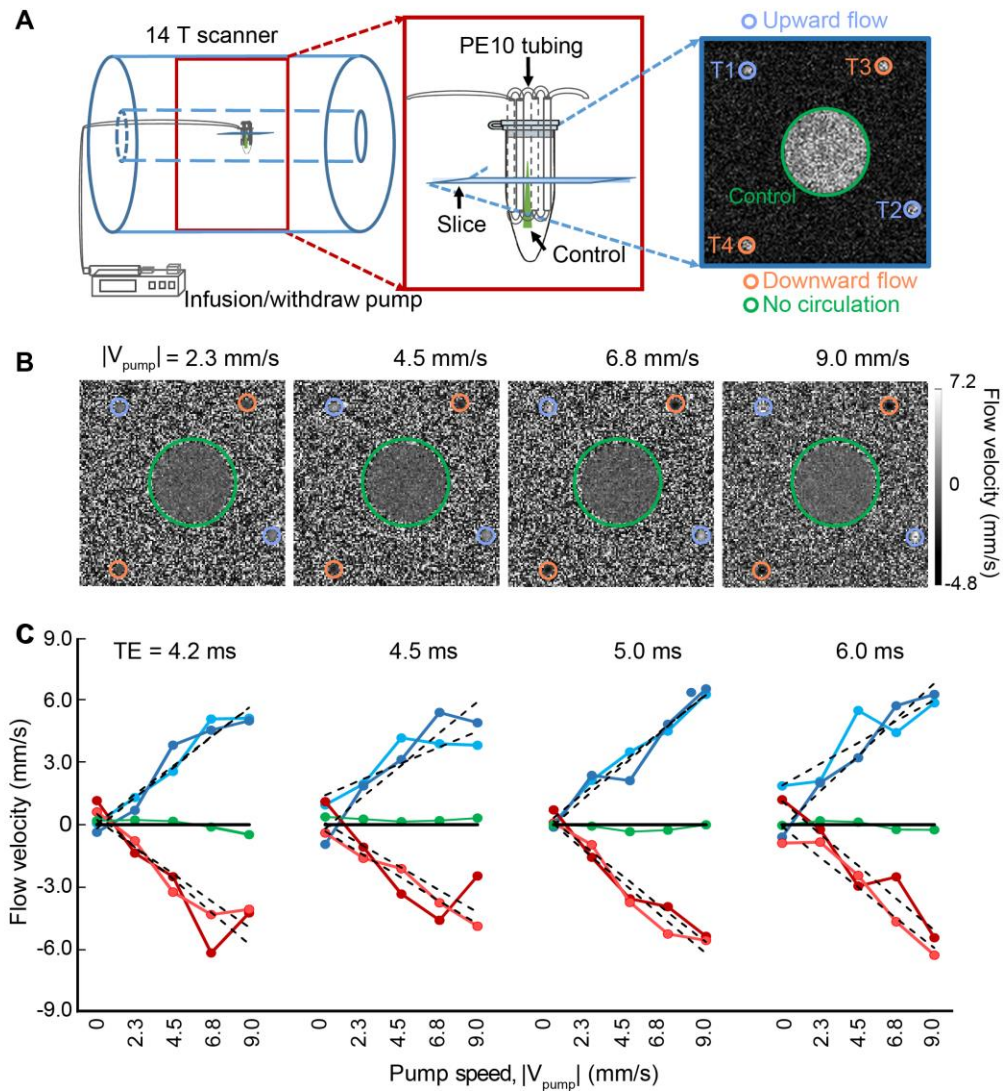
Figure 1. *In vitro* flow velocity measurements with phase-contrast (PC)-MRI. A. Schematic drawing of the phantom experimental flow chamber in the 14.1 T scanner. An expanded image (red box) shows the circulatory system constructed of capillary tubes. A representative fast low angle shot (FLASH) MRI image (blue box), 500 μm in thickness, shows the capillary positions. regions of interest (ROIs) T1 and T2, contoured in purple, indicate the upward flow. ROIs T3 and T4, in orange contour, indicate the downward flow. The green contour indicates the stagnant fluid. **B**. Representative images with different flow velocity in the capillaries T1 to T4 in panel A. (echo time) TE = 5.0 ms for all panels. **C**. The plot of flow velocity estimates from the five ROIs with different TEs, as marked, and different pump rates, as indicated and marked in panel B. The dotted lines correspond to a linear fitting for velocity measurements of different ROIs.

19

484

485

486
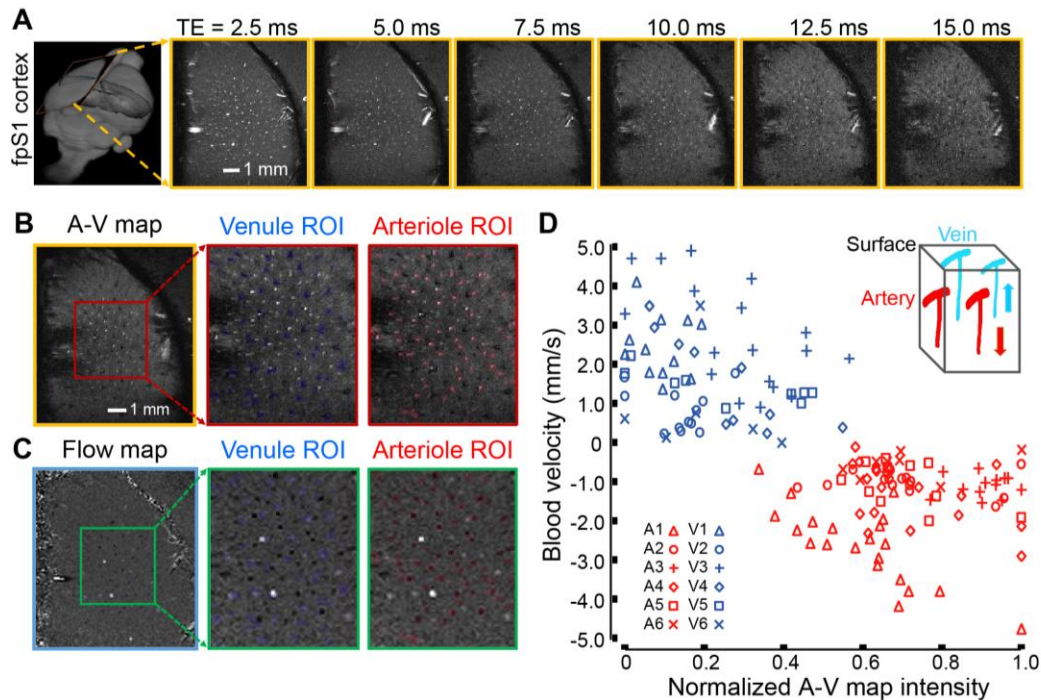
Figure 2. Single-vessel flow velocity measurement. A. Representative 2D multi-gradient echo (MGE) slices (yellow boxes) from a deep layer of the primary forepaw somatosensory cortex (first frame) at different TEs, as indicated. **B.** The 2D arteriole-venule (A-V) map (yellow box) derived from the images with different TEs in panel A, arterioles and venules appear as bright and dark voxels, respectively. The expanded views (red boxes) show individual venules, i.e., black voxels marked in blue, and arterioles, i.e., white voxels marked in red. **C.** The vectorized flow velocity map (blue box) from the same 2D MGE slice in panel B. The expanded views (green boxes) show the individual venules, i.e., white dots with positive velocity, and arterioles, i.e., black dots with negative velocity. Note that 2 bright dots are caused by the "over-flowed" velocity beyond the maximal velocity, i.e., the velocity encoding (Venc) parameter, defined in the PC-MRI sequence, which could be not correctly estimated. **D.** Scatter plot of the flow velocities from individual arterioles and venules as the function of the normalized signal intensities of each vessel in the A-V map of panel B, data from 6 rats as indicated. Insert shows the blood flow direction of arterioles and venules in the forepaw somatosensory cortical region.

20
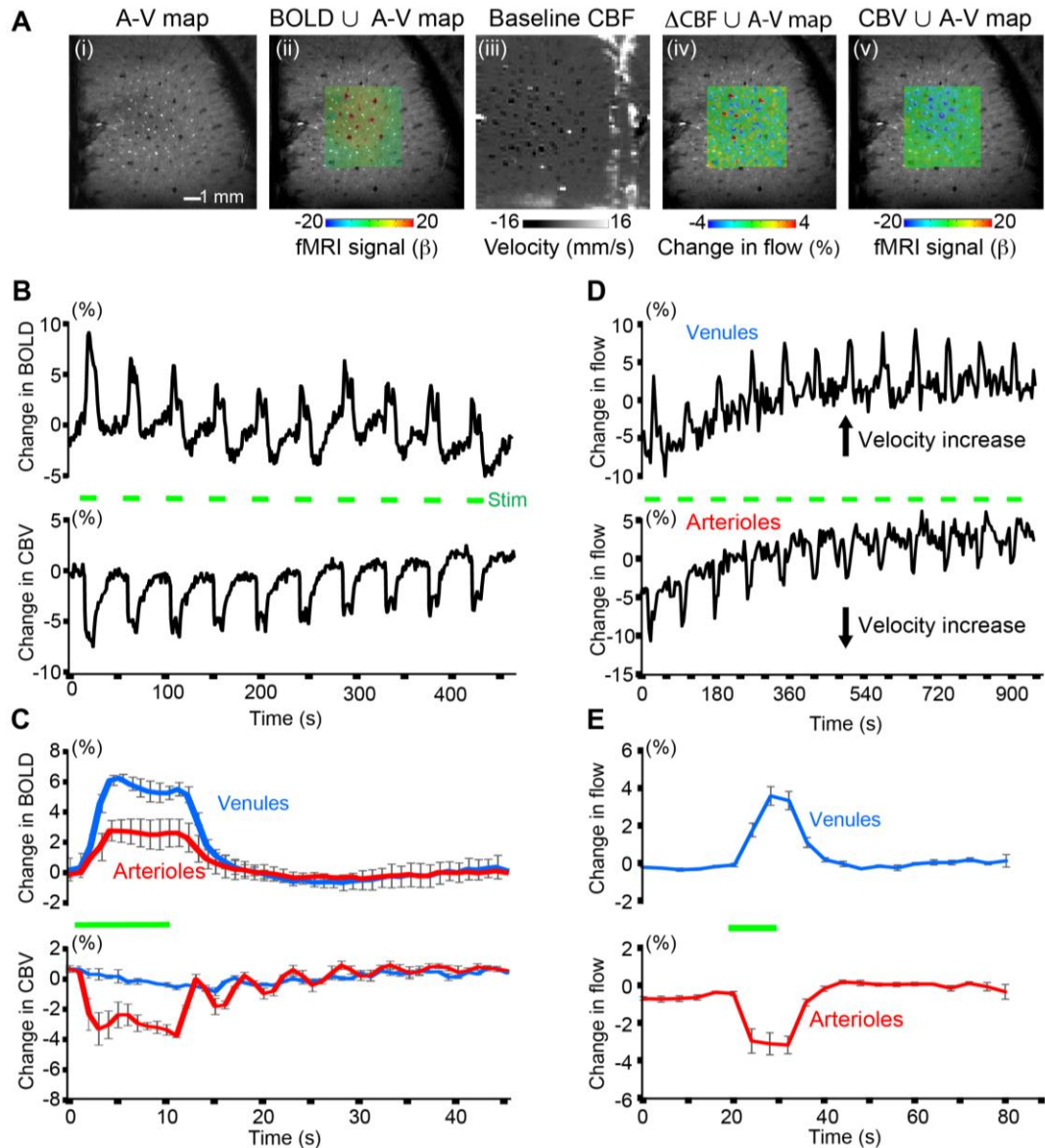
Figure 3. Maps of task-related hemodynamic signals with BOLD, CBV, and CBF-fMRI. A. Different MRI measurement strategies on the same 2D slice. From left to right: (i) The single-vessel A-V map acquired with the MGE method; (ii) The evoked balanced steady-state free precession (bSSFP)-based BOLD-fMRI signal, within the green subregion, on top of the A-V map; (iii) the PC-MRI map of baseline CBF; (iv) the change in CBF on top of the A-V map with an increased flow velocity corresponding to brighter voxels for venules and darker voxels for arterioles; and (v) the evoked bSSFP-based CBV-fMRI signal on top of the A-V map. **B.** The time courses of the evoked bSSFP-BOLD and CBV-fMRI with the block-design paradigm from the venules and arterioles shown in panel A. Forepaw stimulation pulse of 330 µs in width and 1 mA in amplitude delivered at 3 Hz for 10 s. **C.** The averaged time courses of the fractional change for

21

512   the evoked BOLD and CBV signals from the venule and arteriole ROIs from different rats (mean

513   ± SEM, the green bar shows stimulation duration). The peak BOLD values of venule are

514   significantly higher than those of arteriole (5 rats, p = 0.009), while the peak CBV values of

515   arteriole are significantly higher than those of venule (3 rats, p = 0.028). **D.** The time courses of

516   the evoked CBF changes from the arteriole and venule ROIs show increased velocity from both

517   arterioles and venules with the block–design, 10 s duration stimulation paradigm. **E.** The

518   averaged time courses of the evoked CBF changes show the velocity increase from both arteriole

519   and venule ROIs with the block–design stimulation paradigm from 4 rats (mean ± SEM, the green

520   bar shows stimulation duration).

Supporting information

521

522
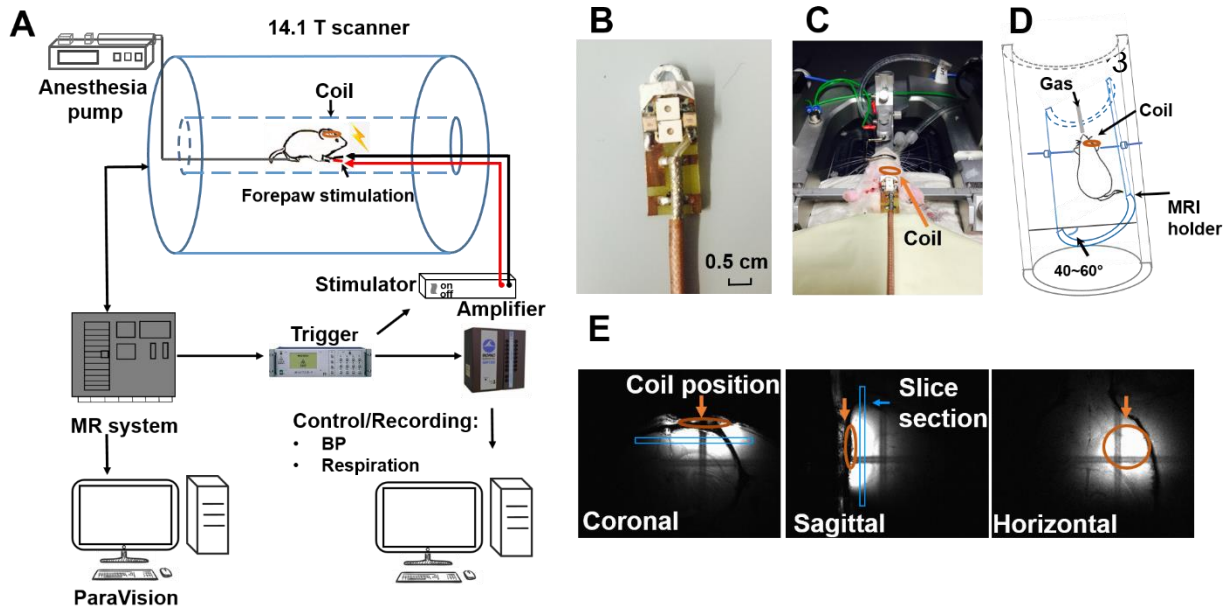

524

525

526

527

528

529

Figure S1. The preparation of *in vivo* experiment for the PC-MRI in 14.1 T.

A. The flow chart of the *in vivo* experiment in the 14.1 T scanner.

B. Photograph of the custom-made transceiver surface RF coil.

C. Photograph of the coil position: the coil is glued to the rat skull.

D. The schematic drawing of the rat position inside the MRI holder.

E. Representative images from different views of the FLASH MRI show the ideal coil position.
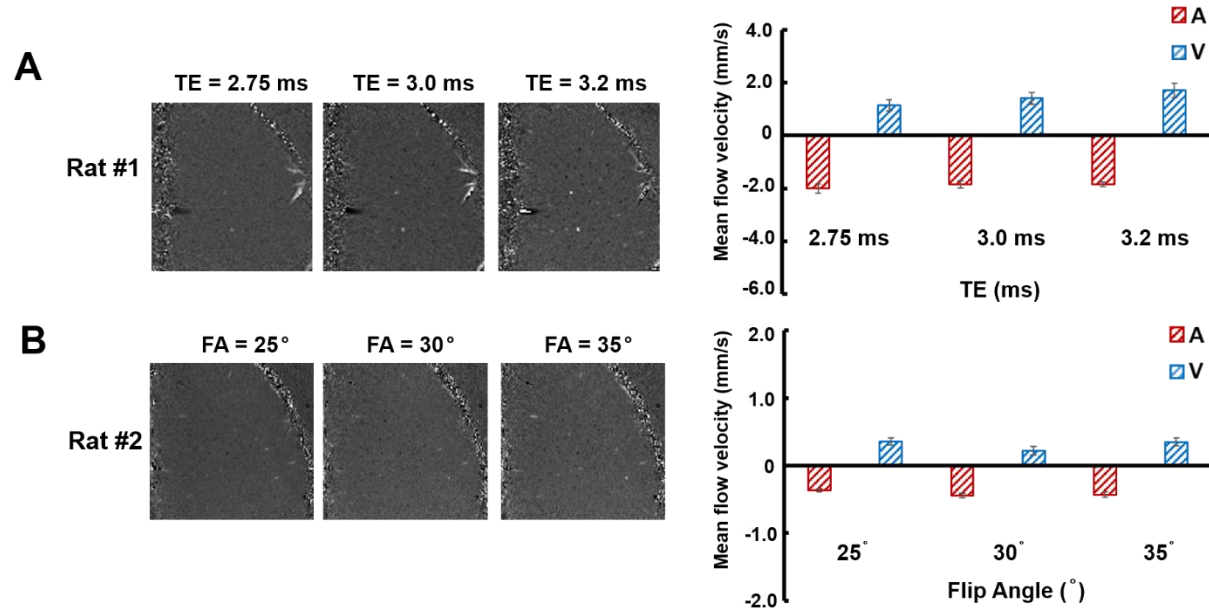
Figure S2. Phase images from the different representative rats with different TEs and flip angles.

A. Phase images from a representative rat with different TEs, i.e., 2.75, 3.0, and 3.2 ms. The right panel shows the mean blood flow velocity (mean ± SEM) from left images with $N_{Arteriole}$ = 48 and N_{Venule} = 22.

B. Phase images from a representative rat with different flip angles, i.e., 25°, 30°, and 35°. The right panel shows the mean blood flow velocity from left images with $N_{Arteriole}$ = 38 and N_{Venule} = 14.
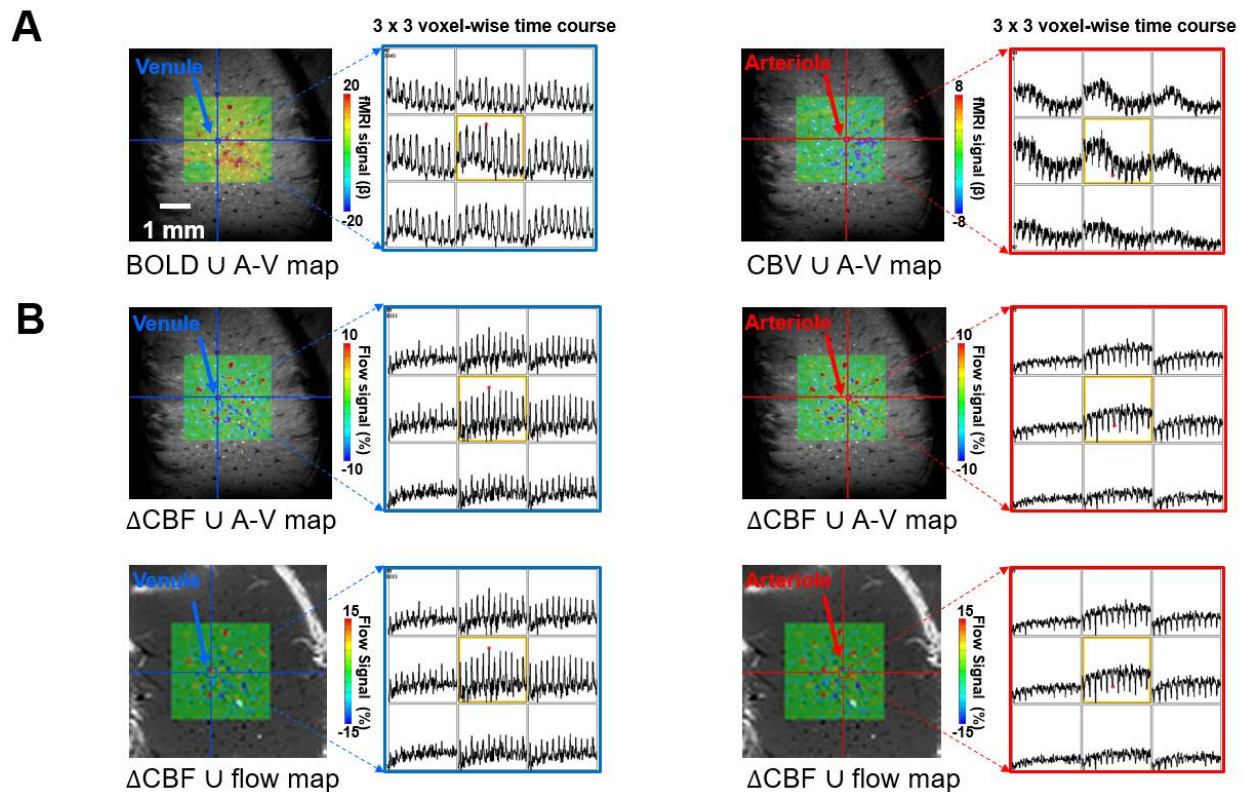
Figure S3. The bSSFP-based single-vessel BOLD/CBV-fMRI and the PC-MRI based single-vessel dynamic flow measurement from a representative rat.

A. The evoked bSSFP-based BOLD- (left) and CBV- (right) fMRI maps overlaid on the same A-V map from a representative rat, with the voxel-wise time courses from the ROIs of individual venule (blue arrow) and arteriole (red arrow) (10 s on and 35 s off for 10 epochs plotted in a 3 x 3 matrix).

B. The evoked CBF maps overlaid on both A-V map (upper panel) and PC-based flow map (lower panel) from the same representative rat. The voxel-wise time courses of CBF changes from the same ROIs of individual venule (blue arrow) and arteriole (red arrow) (10 s on and 50 s off for 12 epochs plotted in a 3 x 3 matrix).

Supplementary Movie Legends

Movie 1. The bSSFP-based single-vessel BOLD/CBV-fMRI and the PC-MRI based single-vessel dynamic flow measurement in the rat cortex.

The upper panel shows the evoked bSSFP-based BOLD- (left) and CBV- (right) fMRI maps overlaid on the 2D A-V map with 50 x 50 μm^2 in-plane and the time course from a single voxel located at a representative venule (blue arrow) and arteriole (red arrow) (10 s on and 35 s off for a total of 45 s time window with TR = 1 s). The middle panel shows the evoked CBF maps overlaid on the same 2D A-V map from the same individual venule (left) and arteriole (right), of which the CBF-fMRI maps were registered to match the 2D A-V map at the 50 x 50 μm^2 resolution, as well as the time courses of the PC-based flow velocity dynamic changes from same voxels identified as the upper panel (10 s on and 50 s off for a total of 60 s time window with TR = 4 s). The lower panel shows the evoked CBF maps overlaid on the PC-based flow map with 100 x 100 μm^2 resolution and the time course from the voxels located at the representative venule (left) and arteriole (right). Note that the venule is a bright voxel and arteriole is a dark voxel in the flow map, which is opposite to the A-V map and also the slightly different time course due to the altered spatial resolution.
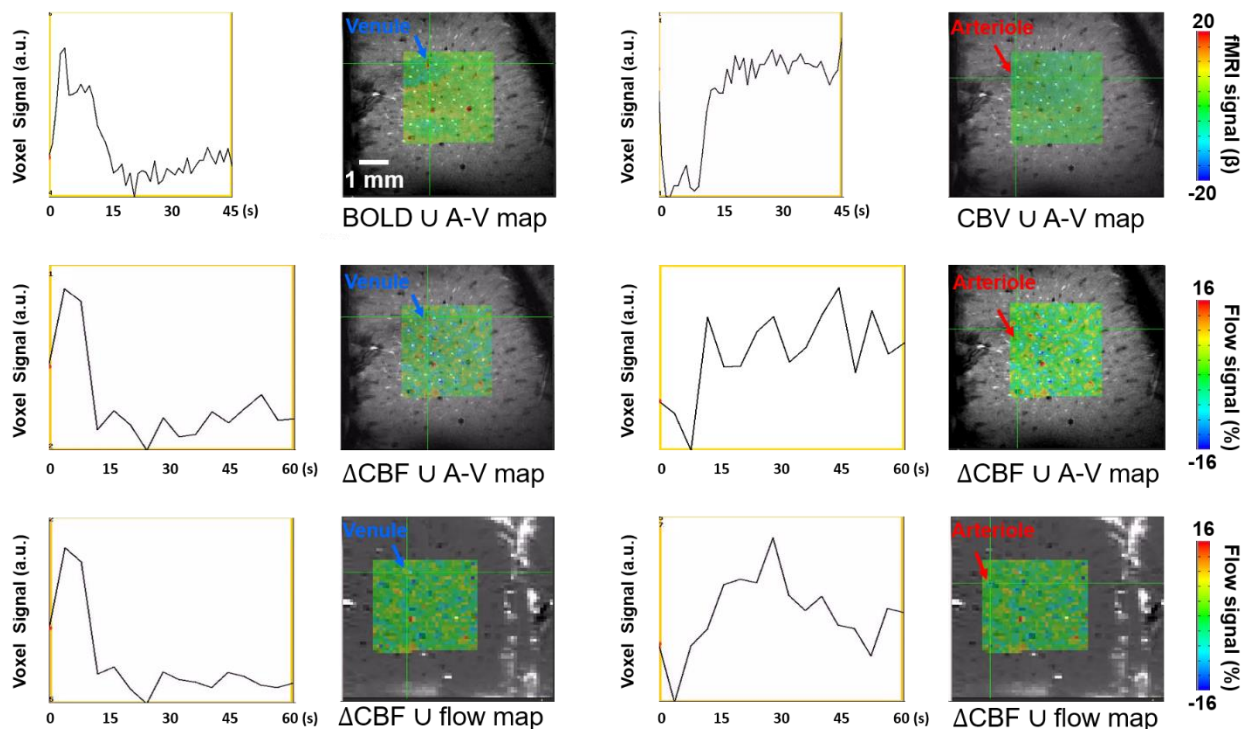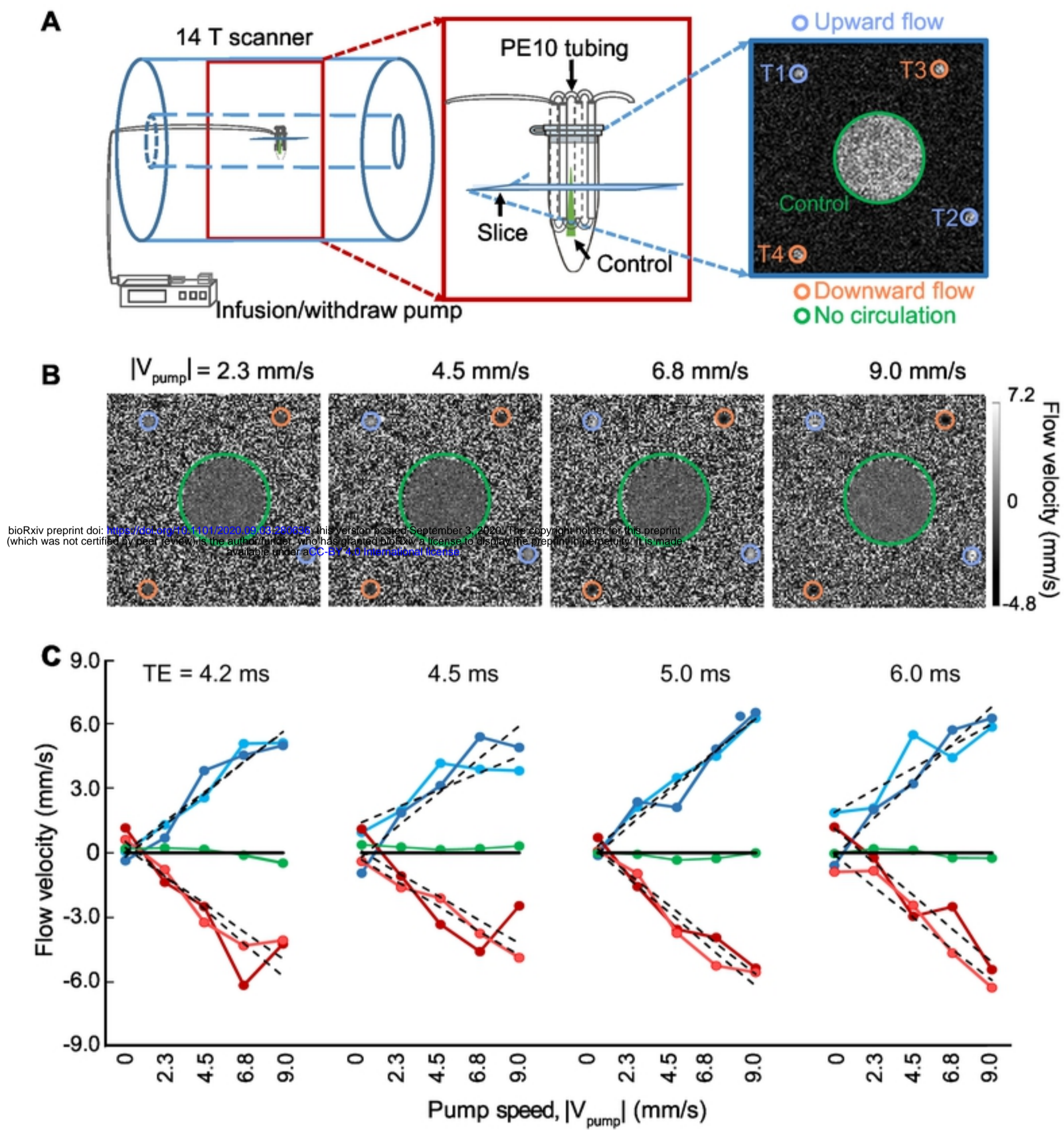
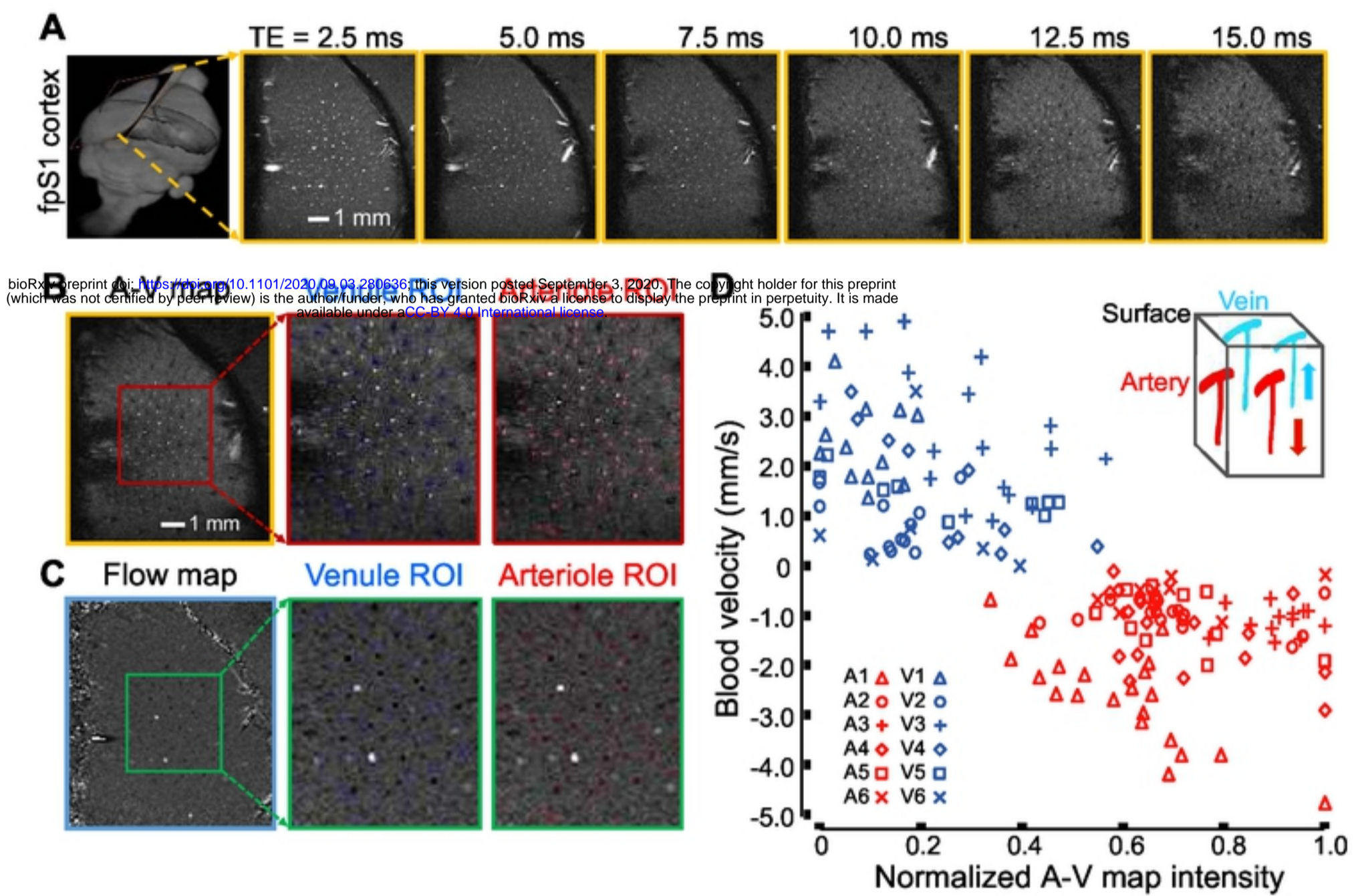Figure 1. Chen, Jiang, Choi, Pohmann, Scheffler, Kleinfeld and Yu

Figure 1

Figure 2. Chen, Jiang, Choi, Pohmann, Scheffler, Kleinfeld and Yu

Figure 2

A

A-V map (i) — 1 mm

BOLD ∪ A-V map (ii)
-20 ▬ 20
fMRI signal (β)

Baseline CBF (iii)
-16 ▬ 16
Velocity (mm/s)

ΔCBF ∪ A-V map (iv)
-4 ▬ 4
Change in flow (%)

CBV ∪ A-V map (v)
-20 ▬ 20
fMRI signal (β)

B

Change in BOLD (%)

Change in CBV (%)

Stim

Time (s)

C

Change in BOLD (%) — Venules, Arterioles

Change in CBV (%)

Time (s)

D

Change in flow (%) — Venules, Velocity increase

Change in flow (%) — Arterioles, Velocity increase

Time (s)

E

Change in flow (%) — Venules
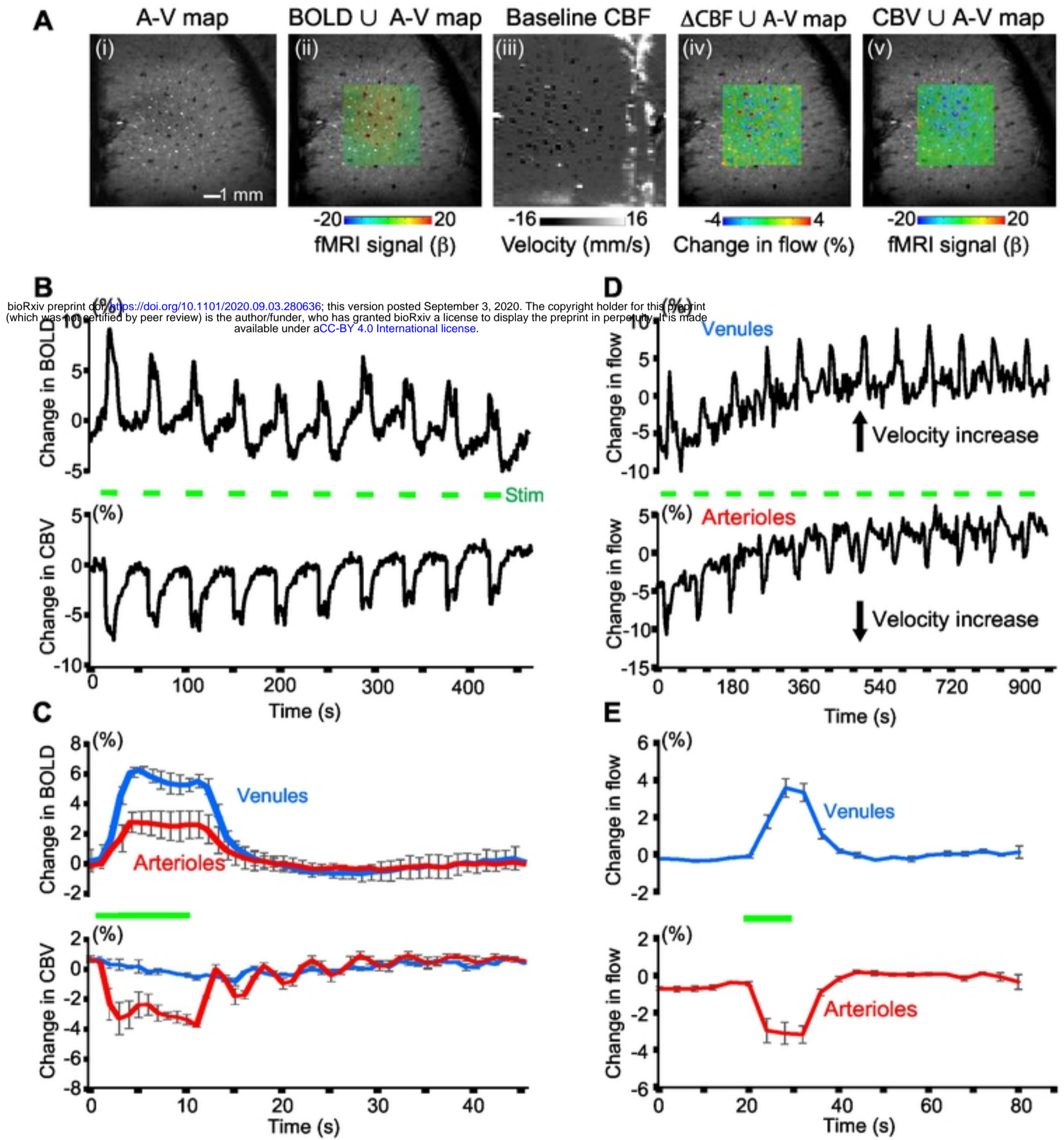
Change in flow (%) — Arterioles

Time (s)

Figure 3. Chen, Jiang, Choi, Pohmann, Scheffler, Kleinfeld and Yu

Figure 3